Extended Conjugation Refining Carbon Nitride with Thermodynamically Boosted Photocatalytic H_2O_2 Production and Application for Hypoxic Tumor Therapy

Jin Ma,[a] Xiaoxiao Peng,[a] Zhixin Zhou,[a] Hong Yang,[a] Kaiqing Wu,[a] Zhengzou Fang,[b] Dan Han,[a] Yanfeng Fang,[a] Songqin Liu,[a] Yanfei Shen,[b] Yuanjian Zhang[a]*

[a]Jiangsu Engineering Laboratory of Smart Carbon-Rich Materials and Device, Jiangsu Province Hi-Tech Key Laboratory for Bio-Medical Research, School of Chemistry and Chemical Engineering, Southeast University, Nanjing 211189, China, E-mail: Yuanjian.Zhang@seu.edu.cn

[b]Medical School, Southeast University, Nanjing 210009, China

Abstract

Artificial photosynthesis offers a promising strategy to efficiently produce hydrogen peroxide (H_2O_2)-not only an essential industrial chemical but also a promising intermediate product in tumor therapy. However, the rapidly consumed dissolving O_2, the competition between oxygen reduction reaction (ORR) and hydrogen evolution reaction (HER), and poor activity of water oxidation reaction (WOR) in the photocatalytic processes greatly restrict the efficiency of photocatalytic H_2O_2 production. In this study, we report a well-defined metal-free C_5N_2 photocatalyst for efficiently H_2O_2 production without sacrificial reagents and stabilizers both in normoxic and hypoxic systems. Experimental and computational investigations indicated that the strengthened delocalization of π−electrons by imine facilitated the formation of electronic structure matching H_2O_2 production both at the conduction band and valence band in thermodynamics, thus an efficient electron-hole separation and the realistic redox selectivity were successfully enabled. Under simulated solar irradiation, C_5N_2 achieved an apparent quantum efficiency of 15.4% at 420 nm together with a solar-to-chemical conversion efficiency of 0.55% for H_2O_2 synthesis, among the best H_2O_2 production photocatalysts in normoxic systems. More interestingly, due to the dual channels of H_2O_2 generation, C_5N_2 could efficiently remove hypoxia restriction and further induce more severe cell damage in photodynamic therapy (PDT). Our findings provided essential insights into the design and synthesis of the dual-channel H_2O_2 production photocatalysts at the molecular level and would pave more broad applications of photocatalytic H_2O_2 production.

Keywords: photocatalysts, carbon nitrides, hydrogen peroxide, non-sacrificial, photodynamic therapy, hypoxic tumor

Introduction

As an important environmentally friendly oxidant, hydrogen peroxide (H_2O_2) has drawn increasing attention for broad industrial applications [1-4]. Except for the conventional renewable clean fuel, chemical healthy synthesis catalyzer and environmental treatment disinfectant, H_2O_2 becoming a promising intermediate-product in life analysis therapy due to its noninvasive features, high efficiency, and ideal accuracy [5-10]. It has been reported that H_2O_2 can be catalyzed to produce O_2 to alleviate O_2 deficiency in the hypoxic tumor microenvironment [11,12]. In addition, H_2O_2 can be used as a green raw material to produce particularly plenty of cytotoxic oxygen-related species via the Fenton reaction for cancer treatment [13-15]. Along with this increasing demand for H_2O_2, many pioneering strategies have been developed for sustainable production technologies.

Currently, H_2O_2 is manufactured by the high energy-consuming and substantial wasting anthraquinone method [16]. it is imperative to develop an alternative approach for H_2O_2 manufacture based on an efficient, economical, and environmentally-friendly process. Based on them, artificial photosynthesis using semiconductor materials has attracted significant interest [17,18]. Although plenty of pioneering studies investigating H_2O_2 production in several particulate systems have been reported, such as foreign chemical doping, surface defects controlling, various heterogenization and molecular architecture modulation, most of them still exhibited general, relatively poor efficiencies of H_2O_2 production [6-8,18-21]. The ineffective hole scavenging via water oxidation and the resulting charge recombination often necessitates the addition of organic electron donors [22,23]. Besides, low selectivity toward H_2O_2 synthesis via two-electron O_2 reduction compared to the four-electron reduction of O_2 or two-electron H_2 evolution required manipulating noble metallic sites as cocatalysts to improve both the activity and selectivity of H_2O_2 production [19,24-26]. However, the excessive addition of sacrificial agents and heavy metal ions not only raises the consumption of raw materials but also increases the subsequent purification difficulty of H_2O_2 in industrial production, which is more adverse to the development of efficient H_2O_2 application in life and health field, such as cancer therapy [20,24].

For the highly efficient production and wide application of H_2O_2, metal-free semiconductors, as best exemplified by polymeric carbon nitrides (pCNs) of graphitic structure, have emerged many pioneering strategies for electronic structures engineering to enhance spatially separating redox with various molecular structures

or/and foreign dopants [28-32]. They have been envisaged as promising photocatalysts for the light-driven synthesis of H_2O_2 without any sacrificial reagents. The rich active sites of imine (C=N) in triazine or heptazine repetitive units facilitate good catalytic activity in receiving photogenerated electrons for O_2 reduction, and the intrinsic oxidative active sites can capture the photogenerated holes for water oxidation [34-35]. Both of them significantly suppressed the recombination of photogenerated charge and formatted a high density of electrons/holes reactive centers. Nonetheless, the reduction of O_2 is still the primary route toward H_2O_2 production for most photocatalysts; meanwhile, nearly all pCNs commonly manifest the poor efficiency of H_2O_2 production when no sacrificial reagents or stabilizers are cooperatively used [33-35]. The challenge lies in maintaining the stable existence of rapidly consumed dissolving O_2 and strengthening the ability of water oxidation reaction in the reaction system [22,34-36]. Similar challenges also exist in another essential application of photocatalysis. The O_2 deficiency in the hypoxic tumor microenvironment along with the inefficient electron-hole separation in photocatalysts dramatically limits photodynamic therapy efficacy [38-42]. Therefore, the development of non-sacrificial, novel, efficient visible-light-responsive of photo non-metal semiconductor materials is of particular interest to address the restrictions mentioned above; however, it has been rarely reported to our knowledge.

Herein, we report the synthesis of graphitic C_5N_2 with a conjugated imine (C=N) linkage via Schiff's base reaction in a liquid phase [43]. Simply by varying reaction time, the degree of polymerization could be successfully tuned, making the molecular weight of pCN be quantitatively characterizable by gel permeation chromatography (GPC) for the first time. More interestingly, due to the strengthened delocalization of π−electrons by imine, the as-obtained C_5N_2 demonstrated the appropriate conduction and valence band position in the pCN family, promoting an efficient electron-hole separation ability and the realistic redox selectivity by the thermodynamics. As a result, the C_5N_2 exhibits remarkable non-sacrificial photocatalytic H_2O_2 synthesis ability in pure water under both a normoxic and hypoxic environment. The optimized photosynthetic rate of H_2O_2 reached 1550 $\mu M\ h^{-1}$ under one standard sunlight at 298 K in a water and oxygen mixture, which was 298 times higher than that for traditional g-C_3N_4 (5.2 $\mu M\ h^{-1}$). The apparent quantum efficiency (AQE) of C_5N_2 at 420 nm was more than 15.4 %, and the solar-to-chemical conversion (SCC) efficiency of C_5N_2 reached as high as 0.55%, comparable with the most efficient water-splitting photocatalysts [8,22,32-35]. Thanks to

the unusually high efficiency of photocatalytic H_2O_2 production in the hypoxic environment without any sacrificial agents, C_5N_2 was further successfully applied to photodynamic hypoxic tumor therapy with very appealing performances. Our findings revealed that disclosure of critical functions of linkers in electronic structure modulation for pCN would greatly enrich the intriguing properties of carbon nitrides family and expand the scope of their prospective applications.

Results and discussion
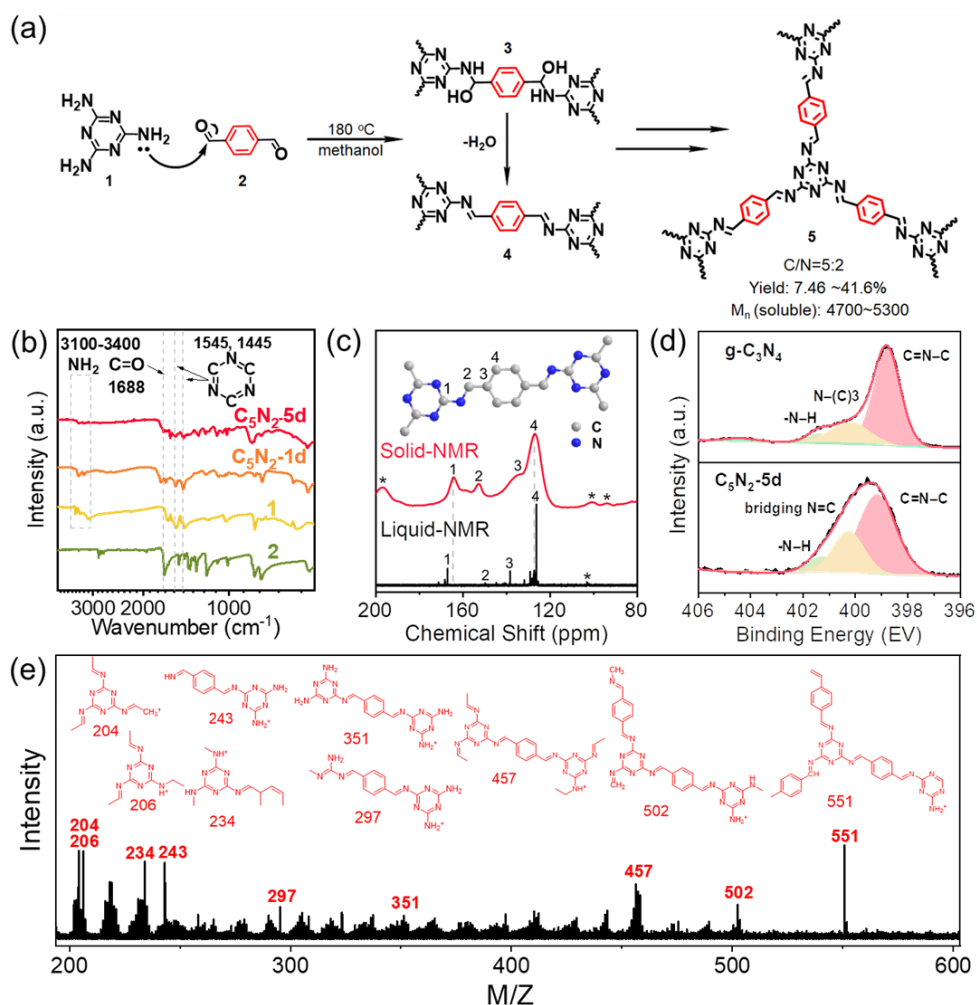
Figure 1. (a) Reaction pathway of imine formation in the synthesis of C_5N_2 (**5**) from melamine (**1**) and p-phthalaldehdye (**2**) through Schiff base reactions. (b) FT-IR spectra of C_5N_2-5d, C_5N_2-1d, **1**, and **2**. (c) Solid-state ^{13}C NMR spectra of the insoluble part and liquid-state ^{13}C NMR spectra of the dissoluble part of C_5N_2-5d. (d) High-resolution N_{1s} XPS spectra of C_5N_2-5d and traditional g-C_3N_4. (e) LDI mass spectrum of C_5N_2-5d and possible assignments.

4

Fig. 1a illustrates the general principle of using melamine (**1**) and p-phthalaldehdye (**2**) as the monomers in an idealized molar ratio of 3:2 via the Schiff's base reaction with the intermediate **3** and **4** to synthesize C_5N_2 (**5**). To understand the reaction kinetics and polymerization degree, the influence of reaction time on C_5N_2 formation was explored. It is worth mentioning that the yield of insoluble solid products gradually increased and reached a plateau with the increase of the reaction time up to 5 days (**Table S1**). Moreover, it was found that superacid catalysts (e.g. Sc(OTf)$_3$) could accelerate the formation and exchange of double-bond linkage between aromatic aldehydes and primary amines, thus improving the yield up to 3 times [44]. From the FT-IR spectra of the solid products collected at different time intervals (C_5N_2-X, X stands for the reaction time in day), the relative intensity of characteristic vibration peaks of NH$_2$ (3100-3500 cm^{-1}) and C=O (1688 cm^{-1}) groups gradually weakened (Fig. 1b and S1), indicating the stepwise consuming of the monomers during the Schiff-base polymerization processes. Some peaks at 1545 cm^{-1} and 1445cm^{-1} that were assigned to characteristic vibrations of the aromatic C=N heterocycles, were also observed in C_5N_2-1d and C_5N_2-5d, indicating the retention of the triazine unit during the Schiff-base reaction. Nonetheless, the stretching vibration of the imine (C=N) linkage was inapparent, which was supposed to be overlapped by that of the aromatic C=N heterocycles. The combustion elemental analysis verified (**Table S2**) that the C/N molar ratio gradually increased with the longer reaction times and finally reached a plateau. Notably, the C/N molar ratio of C_5N_2-5d (2.52), the highest one in this study, was very close to the theoretical value of 2.5, a strong evidence of the successful Schiff-base reaction for C_5N_2 preparation (Fig. 1a). The surface area of C_5N_2-5d (10.717 m^2 g^{-1}, Fig. S2) is only about 1/3 of C_5N_2-3d (27.818 m^2 g^{-1}), also indicating that the increasing degree of polymerization.

Solid-state ^{13}C NMR spectrum of C_5N_2-5d solid (Fig. 1c) was further used to confirm the successful synthesis of C_5N_2. Notably, the C (1) atoms in triazine units at 164.5 ppm, generally, were observed at lower chemical shifts due to the strengthened delocalization of $\pi-$electrons by imine in compared to that of **1** (Fig. S3). The 136.3 and 127.2 ppm confirmed the C (3) and C (4) atoms in the resolved resonances for peripheral phenyl ring units, respectively, almost identical to **2**. Moreover, the disappearance of the peak at 193.5 ppm in ^{13}C spectrum and the peak at 10.1 ppm in ^{1}H of **2** in C_5N_2 (Fig. 1c and S2) were noted, indicating the complete depletion of the aldehyde carbonyl in **2**. More interestingly, some C_5N_2 oligomer was also found in the decanted supernatant after

careful separation and purification. Thanks to good solubility, the liquid-state ^{13}C NMR spectrum in methanol-d4 gave peaks with a much narrower full width at half maximum (FDHM), indicative of a higher resolution compared with the solid-state one (Fig. 1c). The sharp peaks with chemical shifts at 126.0 and 138.4 ppm can be more readily assigned to the peripheral phenyl ring C (4) and C (3) atoms. And, the peak at 167.1 and 150.1 ppm were ascribed to the C (1) atom signals from the triazine ring and C (2) atom signals of the conjugated imine linkage (C=N), further validating the analysis of the solid-state NMR data.

More information on the chemical structure of C_5N_2 was obtained by X-ray photoelectron spectrum (XPS) and laser desorption/ionization (LDI) mass spectrum. Fig. 1d showed the high-resolution N_{1s} XPS spectra of traditional g-C_3N_4 and C_5N_2, which were deconvolved into three peak components of C=N-C bonding, i.e., the tertiary nitrogen N–(C)3 and the bridging N–H, respectively. Due to formating the bridging N=C bond, the N_{1s} XPS peak positions were altered from those in g-C_3N_4; namely, the peak at 400.9 eV can be ascribed to the bridging N=C and the peak for the tertiary nitrogen N–(C)3 shifted to 399.9 eV. High-resolution C_{1s} XPS spectra (Fig. S4) also revealed similar information. Notably, due to the high solubility, the C_5N_2 oligomer was measurable by GPC, one of the most popular and versatile analytical techniques available for understanding and predicting polymer performance. The average molecular weight distribution of 4700-5300 was obtained for the C_5N_2-5d oligomer (**Table S3**), indicative of approximately eight triazine repetitive units. In this sense, the more condensed insoluble C_5N_2-5d should have more triazine repeating motifs. Despite still appealing for more future exploitation, to our knowledge, this is the first quantitative measurement of molecular weights for the carbon nitride family since most as-synthesized carbon nitrides are insoluble and practically inapplicable by GPC. More interestingly, the LDI mass spectrum of C_5N_2-5d (Fig. 1e) demonstrated m/z peaks attributable to the ablation products of the repetitive imidazole units of different link manners in C_5N_2-5d. Therefore, the proposed C_5N_2 with conjugated linkage was successfully synthesized by the Schiff's base reaction.
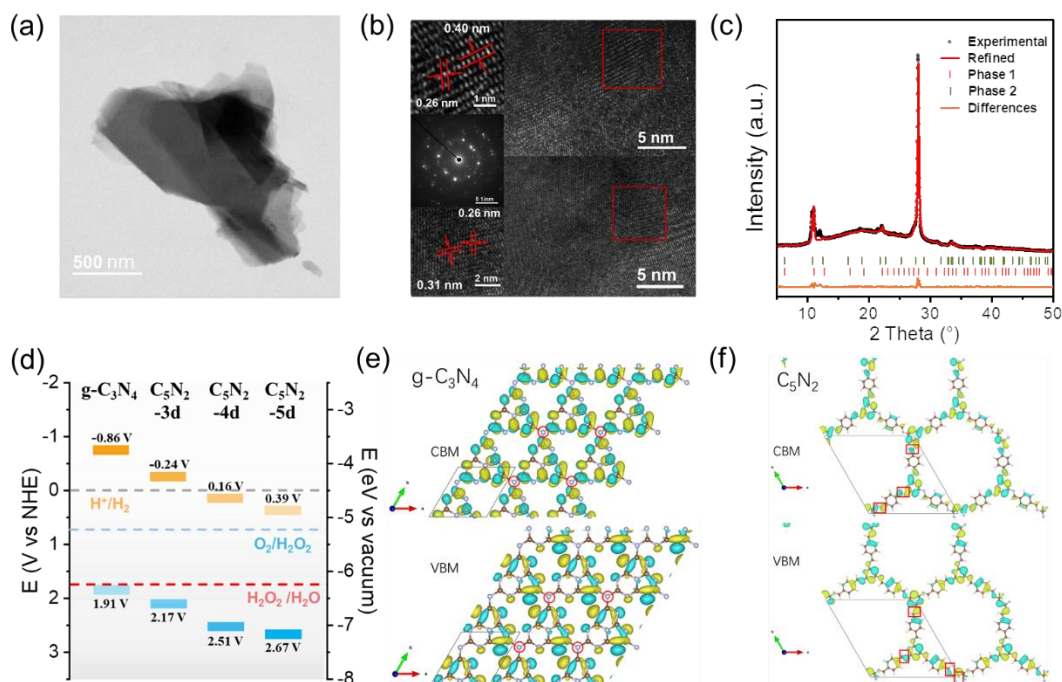
Figure 2. (a) TEM and (b) High-Resolution TEM (HR-TEM) and Fast Fourier transform (FFT) images of C_5N_2-5d. Inset: HR-TEM image from the red square marked area. (c) Experimental and Pawley-refined PXRD patterns of C_5N_2-5d. (d) Calculated band structure of C_5N_2 and g-C_3N_4 by UV−vis absorption and XPS VB scan spectra. The simulated HOMO-LUMO electronic structure distribution of (e) g-C_3N_4 and (f) C_5N_2 by DFT calculations.

The morphology of the C_5N_2-5d was studied with TEM, which demosntrated a layered texture over a few hundred nanometers (Fig. 2a). The high-resolution TEM image (Fig. 2b) and its corresponding fast Fourier transform (FFT) image of the C_5N_2-5d revealed a locally ordered highly crystalline characteristic. The lattice fringes with a spacing of 0.31 nm, corresponding to the (002) planes of C_5N_2-5d, which consisted with the facet in the XRD pattern. The X-ray diffraction (XRD) pattern (Fig. 2c) of C_5N_2-5d further disclosed minor peaks at 2θ values of 22.1° and 33.4°, corresponding to other lattice fringes in the high-resolution TEM image. Besides, Pawley refinement plot provided good agreement factors for the experimental XRD data. The higher crystallinity indicated the high efficiency of the Schiff-base reaction in the condensation of the carbon nitride framework.

Owing to the strengthened delocalization of π−electrons by imine bonds, the electronic band structures of C_5N_2 were supposed to be significantly altered. The UV-

Vis spectra of C_5N_2 with different polymerization degrees showed a characteristic broad absorption band with a distinctive absorption edge for semiconductors (Fig. S5). The absorption edge gradually increased from 515 to 544 nm, corresponding to the bandgap from 2.42 to 2.28 eV, with the increase of the polymerization time. Compared with g-C_3N_4, whose absorption edge was at ca. 447 nm, the absorption edge of C_5N_2-5d red-shifted 97 nm. Likewise, in the photoluminescent spectrum (Fig. S6), the maximum emission of C_5N_2-5d red-shifted over that of g-C_3N_4 by 90 nm. To further estimate the conduction band (CB) and valence band (VB) position of C_5N_2, the VB X-ray photoelectron spectra (VB-XPS) between C_5N_2 and g-C_3N_4 (Fig. S7) and E_{fb} of g-C_3N_4 (Fig. S8) were recorded and compared. As summarized in Fig. 2d, during the gradual narrowing of bandgap with the increase of polymerization time, the downshift of the CB and VB position of C_5N_2 played a predominant role. The CB of C_5N_2 was even exceptionally lower than 0 V vs NHE, which was highly envisioned to drive a highly selective O_2 reduction into H_2O_2 without competitive H_2 evolution in thermodynamics. Thus, the conventional metal-containing cocatalysts were not required anymore.

The DFT calculation of g-C_3N_4 and C_5N_2 was explored to get molecular insights into the significantly altered electronic structure (Fig. S9, S10). As shown in Fig. 2e, the tertiary amines act as nodes, breaking the conjugation over the heptazine rings, making the electrons far less than fully delocalized in the HOMO/LUMO orbitals electronic structure distribution of g-C_3N_4. In contrast, the charge density in imine bonds that was redistributed with increasing conjugation was linked to C_5N_2 units, resulting in the strengthened delocalization of π–electrons (Fig. 2f). Such integral charge accumulations led to the downshifting of the CB and VB and strikingly improved the charge separation efficiency of C_5N_2 [48]. In this sense, the hole- and electron-extraction properties were evaluated by measuring anodic and cathodic photocurrents, respectively, in the presence of an electron donor (triethanolamine, TEOA), assuming the maximum photocurrent can be obtained without any hole- or electron-transfer limitations. As shown in Fig. S11, both anodic and cathodic photocurrents at C_5N_2-5d were less improved with respect to g-C_3N_4 by adding TEOA, indicating superior hole- and electron-extraction proper, which was well consistent with the theoretical results [45,46]. Both theoretical calculations and experimental results collaboratively depicted the critical roles of linkers for repeating triazine motifs in electronic structure modulation, an overlooked fact in previous studies.
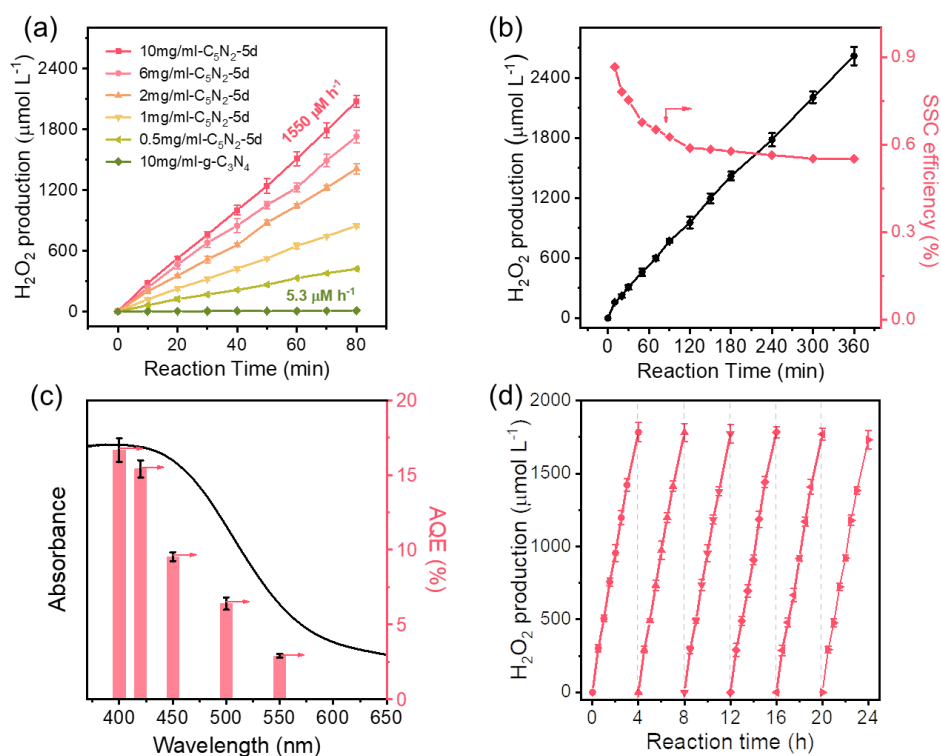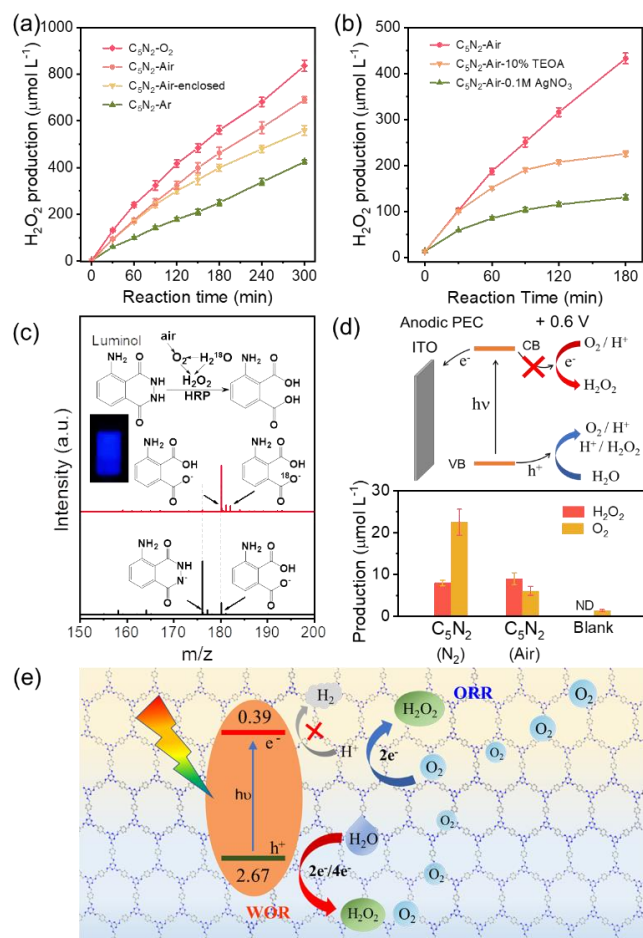
Figure 3. (a) Photocatalytic H_2O_2 production by C_5N_2-5d and g-C_3N_4 at different concentrations in water. (b) Solar-to-chemical conversion (SCC) efficiency of C_5N_2-5d. (c) Apparent quantum efficiency (AQE) of C_5N_2-5d. (d) Stability tests of C_5N_2-5d in photocatalytic H_2O_2 production. Light source: Xenon lamp, $\lambda > 400$ nm, 100 mWcm^{-2}. Error bars represent the standard deviations of three replicate measurements

In principle, semiconductors with lower CB position and higher VB position are highly desirable for participating in direct H_2O_2 generation. The photocatalytic H_2O_2 production performance of the as-prepared catalysts was evaluated under simulated sunlight irradiation ($\lambda > 400$ nm) without any sacrificial agents or stabilizers. Fig. 3a revealed the photocatalytic rate of H_2O_2 in 10 mL water with different amounts of C_5N_2-5d and g-C_3N_4 in 80 min. The 10 mg/mL C_5N_2-5d showed the highest H_2O_2 production rate (1550 μmol L^{-1} per hour) among the samples, which was about 298 times higher than g-C_3N_4 of 10 mg/mL (5.2 μmol L^{-1} per hour). Furthermore, the C_5N_2-5d displayed negligible photocatalytic activity for the hydrogen evolution reaction (Fig. S12). It was verified that C_5N_2 exhibited the efficient electron-hole separation and highly selective O_2 reduction into H_2O_2 ability [49]. When decreasing the catalyst concentration, the H_2O_2 production rate became lower, confirming that extensive catalyst sites improved the efficiency of H_2O_2 production. Fig. 3b, and c show the SCC efficiency and AQE of

H_2O_2 production over C_5N_2-5d, under the optimal concentration (10 mg/mL) in 150 mL and 80 mL water, respectively. The AQE of C_5N_2-5d at 420 nm was determined to be 15.4% by monochromated light irradiation and the SSC efficiency of C_5N_2-5d reached as high as 0.55% in an oxygenated environment, among the most efficient metal-free photocatalysts for non-sacrificial H_2O_2 production. Besides, the H_2O_2 production rate of C_5N_2-5d was well maintained after several repeated cycles, suggesting its good stable catalytic performance (Fig. 3d).


Figure 4. (a) Photocatalytic activity H_2O_2 production of C_5N_2-5d with different concentrations of dissolved oxygen. (b) Photocatalytic activity H_2O_2 production of C_5N_2-5d with an electron acceptor ($NaIO_3$, 0.1 M) or an electron donner (TEOA, 10% v/v). Light source: Xenon lamp, $\lambda > 400$ nm, 100 mW cm^{-2}. (c) Mass spectra of luminol before and after oxidation with hydrogen peroxide generated by photocatalytic $H_2^{18}O$ splitting. (d) Photoelectrochemical production of H_2O_2 and O_2 by C_5N_2-5d in N_2 and air-saturated electrolyte. Biased potential: 0.6 V vs Ag/AgCl. Inset: the proposed pathway of charge transfer and reactions. (e) Mechanism of photocatalytic H_2O_2 production by C_5N_2-5d

Water oxidation and oxygen reduction were then investigated separately to understand insights into the unusually high efficiency of photocatalytic H_2O_2 production. For this purpose, the aqueous solutions containing different concentrations of dissolved oxygen (Fig. 4a) were explored. It was found that the photocatalytic H_2O_2 production rate was the highest in the O_2-saturated water and that in Argon (Ar)-saturated solution was still nearly half of that in the O_2-saturated one. Moreover, capping the reactor without the supplemental air during the photocatalytic reaction showed a lower reaction rate of H_2O_2 production than that in an open-air condition. These facts suggested that the O_2 reduction was profound but was not only the major pathway for the H_2O_2 production in our work.

Interestingly, trapping experiments in Fig. 4b showed that not only electron acceptors (e.g., $AgNO_3$) but also electron donors (e.g., TEOA, 10% v/v) made the photocatalytic H_2O_2 production decrease by C_5N_2-5d, indicating the co-existence of water oxidation reaction (WOR) as well. Isotope experiments were further performed to verify the existence of $2e^-$ WOR. It was supposed that when $H_2^{18}O$ was used, $H_2^{18}O_2$ would be produced if $2e^-$ photocatalytic WOR occurred. However, $H_2^{18}O_2$ was unstable and difficult to be detected by mass spectroscopy. To circumvent this problem, the ^{18}O atom in $H_2^{18}O_2$ was transferred into luminol oxide by a well-known oxidation reaction catalyzed by horseradish peroxidase (HRP) that was accompanied by chemiluminescence (Fig. 4c inset). The Liquid chromatography-mass spectra (LC-MS) of the oxidized luminol demonstrated a strong luminol oxide-^{16}O (m/z) peak and a weak luminol oxide-^{18}O (m/z) peak, while the control not, confirming the occurrence of the $2e^-$ WOR.

As $4e^-$ WOR is more favorable in thermodynamics, the photoelectrochemical (PEC) experiments under aerobic and anaerobic conditions were also explored to check the generation of O_2 at the holes or not, using C_5N_2 modified indium tin oxide (ITO) electrodes. An advantage of the PEC method was that under anodic photocurrents, the excited electrons in the conduction band could be collected by the ITO electrode; thus, the interferent O_2 consumption in the conduction band for the detection of generated O_2 in the valence band could be eliminated [50]. As shown in Fig. 4d, O_2 was successfully detected under an anaerobic condition photocatalyzed by C_5N_2-5d using the dissolved oxygen meter, with a concentration ca. three times of H_2O_2. Interestingly, under aerobic conditions, the photocatalytic generation of O_2 was suppressed to a similar level of O_2 production, presumably ascribed to chemical equilibrium. In these

regards, 4e$^-$ WOR should also exist in photocatalytic water oxidation by C$_5$N$_2$-5d. Based on the above characterizations and analyses, H$_2$O$_2$ was not only produced by photocatalytic 2e$-$ ORR and 2e$-$ WOR pathways, but also by photocatalytic 2e$-$ ORR and 4e$-$ WOR routes, in which the O$_2$ generated from 4e$-$ WOR was consumed by the 2e$-$ ORR process to produce H$_2$O$_2$ (Fig. 4f).
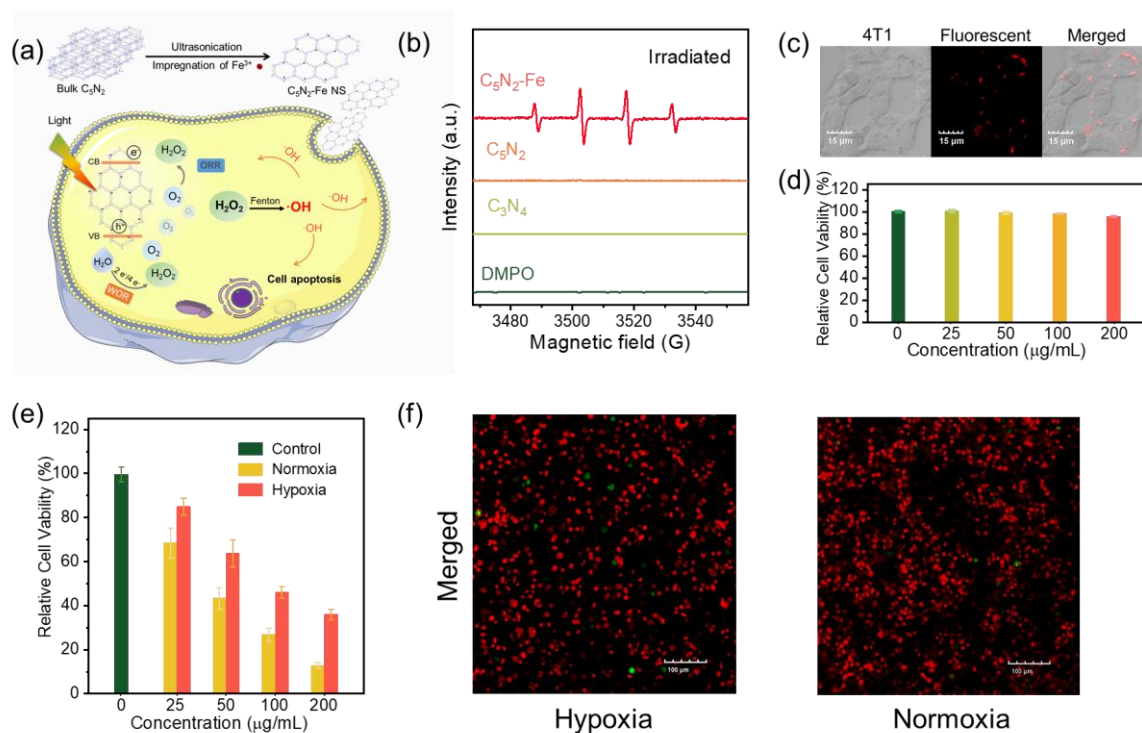
Figure 5. (a) Scheme of C$_5$N$_2$-Fe therapeutic process through simultaneously generating ROS under LED light irradiation in hypoxic environments. (b) ESR spectra of C$_5$N$_2$-Fe NS, C$_5$N$_2$ NPs, g-C$_3$N$_4$ powder, DMPO after irradiation. (c) Confocal fluorescence imaging of 4T1 cells upon incubation with C$_5$N$_2$-Fe-NS. Scale bar: 15 μm. (d) Biocompatibility evaluation of C$_5$N$_2$-Fe-NS upon incubation with 4T1 cells by WST-8. (e) Cell viability assay of C$_5$N$_2$-Fe-NS treated 4T1 cells under the LED light irradiation in hypoxic and normoxic environments. (f) Live/dead double staining of C$_5$N$_2$-Fe-NS treated 4T1 cells under LED light indicated by FDA (green, live cells) and PI (red, dead cells). Scale bar: 100 μm.

It should be noted that the photocatalytic production of H$_2$O$_2$ without sacrificial reagents using metal-free photocatalysts in an oxygen gas-free environment have been rarely reported, but which is central of the next generation of PDT cancer treatment under hypoxic microenvironment. As H$_2$O$_2$ could not be provided direct potent injury

to cancer cells, it is a feasible to utilize Fenton or Fenton-like reaction to generate particularly plenty oxygen-related species via the reaction between Fe^{3+}/Fe^{2+} pair and H_2O_2. In this case, the pristine C_5N_2 were decorated with Fe by the traditional impregnation method [51] and exfoliated into nanosheets by ultrasonication [47] (Fig. S13). We next developed a C_5N_2-based ·OH generator and fluorescence agent for photodynamic hypoxic tumor therapy, which exhibited a commendable tumor inhibition effect (Fig. 5a).

The dynamic light scattering analysis showed Fe-decorated C_5N_2 after ultrasonication exfoliation had a hydrodynamic size of 140 nm, and the transmission electron microscopy (TEM) image confirmed the formation of nanosheets with smaller size compared to the pristine C_5N_2 (Fig. S14). To determine the production of ·OH over different samples, electron spin resonance (ESR) spectroscopies were applied. No evident ESR signals for C_5N_2 nanoparticles (C_5N_2 NPs), g-C_3N_4 powder and DMPO were observed, whereas that for C_5N_2 nanosheets decorated with Fe (C_5N_2-Fe NS) demonstrated typical signals, corresponding to DMPO−·OH adducts under the soft white light irradiated (Fig. S12). Meanwhile, there were no signals for C_5N_2-Fe NS in the dark, whereas free Fe^{3+} ions exhibited typical DMPO−·OH adducts signals, which indicated that free Fe^{3+} were completely complexed with strengthened delocalization of π−electrons (Fig. S15). Besides, the production of ·OH through the Fenton or Fenton-like reaction using coumarin (cou) as a probe was investigated (Fig. S16). The probe displayed a new fluorescence emission enhancement at 455 nm upon the reaction to ·OH. With increased irradiated time, as-produced 7-hydroxy-cou exhibited a gradual amplification of fluorescence intensity with C_5N_2-Fe NS, indicating that the aptitude of the Fenton or Fenton-like reaction could be amplified by the soft white light irradiation.

To investigate the accumulation of the C_5N_2-Fe NS in tumor cells, 4T1 cells were cultured and incubated together, and the fluorescence imaging was then measured. The cytoplasm of the 4T1 cells displayed prominent fluorescence signals in the red channel, leaving the nucleus with no fluorescence This observation indicated that C_5N_2-Fe NS was internalized into the cells with specific localization in the cytoplasm. The invitro cytotoxicity of C_5N_2-Fe NS was accessed in 4T1 cells by 2-(2-Methoxy-4-nitrophenyl)-3-(4-nitrophenyl)-5-(2,4-disulfophenyl)-2H-tetrazolium Sodium Salt (CCK-8) assay. As shown in Fig. 4d, no noticeable adverse effects were observed in cells without any external stimuli after 24 h, indicating the excellent biocompatibility of C_5N_2-Fe NS. Interestingly, the efficacy of the Fenton or Fenton-like reaction was accelerated by the

molecular turbulence created by irradiation. Under soft LED light (λ>400nm, 30 mW/ cm^{-2}) for 30 min, C_5N_2-Fe NS (200 μg/mL) displayed an efficient cell ablation ability (the cell viability of ~12.7%) in normal microenvironment under the photo-driving ·OH generation (Fig. 4c). Compared to that of C_5N_2-Fe NS in hypoxic microenvironment (1% O_2), the viability of 4T1 cells also noticeably decreased to about ~37.5%, exhibiting photo-mediated ·OH generation in hypoxic tumor microenvironment. Meanwhile, fluorescein diacetate (FDA) and propidium iodide (PI) were utilized to stain the live and dead cells, respectively. Live/dead cell staining assay (Fig. 4e) further confirmed the comparable significant cell death caused by C_5N_2-Fe NS in normoxic and hypoxic cell environment under soft LED light irradiation, consistent with the WST-8 tests. The outstanding photocatalytic activity of C_5N_2 in 2e$^-$ ORR and 2e$^-$/4e$^-$ WOR under hypoxic environments exhibited a high potential in the application of tumor therapy (Fig. 4f).

Conclusions

In summary, we report a well-defined metal-free C_5N_2 photocatalyst for selective, efficient and stable H_2O_2 production without any sacrificial reagents and stabilizers in normoxic and hypoxic systems. Our investigations revealed that the strengthened delocalization of π−electrons by imine facilitated the formation of bandgap matching for H_2O_2 production by the thermodynamics, thus promoted an efficient electron-hole separation ability and the realistic redox selectivity. Under simulated solar irradiation, C_5N_2 achieved an apparent quantum efficiency of 15.4% at 420 nm together with a solar-to-chemical conversion efficiency of 0.55% for H_2O_2 synthesis, among the best H_2O_2 production photocatalysts in normoxic systems. Moreover, parallel to industrial H_2O_2 production to address energy and environment challenges, it was confirmed that C_5N_2 could be efficiently removed hypoxia restriction and further induced more severe cell damage for PTD, due to the dual channel property of generating H_2O_2-like radicals. Our findings provided important insights into the design and synthesis of the dual-channel H_2O_2 production photocatalysts at the molecular level and presented rising potentials of metal-free carbon nitride not only for sustainable energy and environments but also for superior PTD therapies in health.

Reference

(1) Xia, C.; Xia, Y.; Zhu, P.; Fan, L.; Wang, H. Direct electrosynthesis of pure aqueous H_2O_2 solutions up to 20% by weight using a solid electrolyte. *Science* **2019**, *366* (6462), 226-231.

(2) Chu, S.; Cui, Y.; Liu, N. The path towards sustainable energy. *Nature Materials* **2016**, *16* (1), 16-22.

(3) Perry, S. C.; Pangotra, D.; Vieira, L.; Csepei, L.-I.; Sieber, V.; Wang, L.; Ponce de León, C.; Walsh, F. C. Electrochemical synthesis of hydrogen peroxide from water and oxygen. *Nature Reviews Chemistry* **2019**, *3* (7), 442-458.

(4) Kim, H. W.; Ross, M. B.; Kornienko, N.; Zhang, L.; Guo, J.; Yang, P.; McCloskey, B. D. Efficient hydrogen peroxide generation using reduced graphene oxide-based oxygen reduction electrocatalysts. *Nature Catalysis* **2018**, *1* (4), 282-290.

(5) Mousavi Shaegh, S. A.; Nguyen, N.-T.; Mousavi Ehteshami, S. M.; Chan, S. H. A membraneless hydrogen peroxide fuel cell using Prussian Blue as cathode material. *Energy & Environmental Science* **2012**, *5* (8).

(6) Wu, Q.; Cao, J.; Wang, X.; Liu, Y.; Zhao, Y.; Wang, H.; Liu, Y.; Huang, H.; Liao, F.; Shao, M.; et al. A metal-free photocatalyst for highly efficient hydrogen peroxide photoproduction in real seawater. *Nature Communications* **2021**, *12* (1).

(7) Shiraishi, Y.; Takii, T.; Hagi, T.; Mori, S.; Kofuji, Y.; Kitagawa, Y.; Tanaka, S.; Ichikawa, S.; Hirai, T. Resorcinol–formaldehyde resins as metal-free semiconductor photocatalysts for solar-to-hydrogen peroxide energy conversion. *Nature Materials* **2019**, *18* (9), 985-993.

(8) Kou, M.; Wang, Y.; Xu, Y.; Ye, L.; Huang, Y.; Jia, B.; Li, H.; Ren, J.; Deng, Y.; Chen, J.; et al. Molecularly Engineered Covalent Organic Frameworks for Hydrogen Peroxide Photosynthesis. *Angewandte Chemie International Edition* **2022**, *61* (19).

(9) Chen, Q.; Feng, L.; Liu, J.; Zhu, W.; Dong, Z.; Wu, Y.; Liu, Z. Intelligent Albumin-MnO_2 Nanoparticles as pH-/H_2O_2-Responsive Dissociable Nanocarriers to Modulate Tumor Hypoxia for Effective Combination Therapy. *Advanced Materials* **2016**, *28* (33), 7129-7136.

(10) Jana, D.; Wang, D.; Rajendran, P.; Bindra, A. K.; Guo, Y.; Liu, J.; Pramanik, M.; Zhao, Y. Hybrid Carbon Dot Assembly as a Reactive Oxygen Species Nanogenerator for Ultrasound-Assisted Tumor Ablation. *JACS Au* **2021**, *1* (12), 2328-2338.

(11) Chen, H.; Tian, J.; He, W.; Guo, Z. H_2O_2-Activatable and O_2-Evolving Nanoparticles for Highly Efficient and Selective Photodynamic Therapy against

Hypoxic Tumor Cells. *Journal of the American Chemical Society* **2015**, *137* (4), 1539-1547.

(12) Kim, J.; Cho, H. R.; Jeon, H.; Kim, D.; Song, C.; Lee, N.; Choi, S. H.; Hyeon, T. Continuous O_2-Evolving $MnFe_2O_4$ Nanoparticle-Anchored Mesoporous Silica Nanoparticles for Efficient Photodynamic Therapy in Hypoxic Cancer. *Journal of the American Chemical Society* **2017**, *139* (32), 10992-10995.

(13) Tang, Z.; Liu, Y.; He, M.; Bu, W. Chemodynamic Therapy: Tumour Microenvironment-Mediated Fenton and Fenton-like Reactions. *Angewandte Chemie International Edition* **2019**, *58* (4), 946-956.

(14) Liu, G.; Zhu, J.; Guo, H.; Sun, A.; Chen, P.; Xi, L.; Huang, W.; Song, X.; Dong, X. Mo_2C-Derived Polyoxometalate for NIR-II Photoacoustic Imaging-Guided Chemodynamic/Photothermal Synergistic Therapy. *Angewandte Chemie International Edition* **2019**, *58* (51), 18641-18646.

(15) Chen, Q.; Yang, D.; Yu, L.; Jing, X.; Chen, Y. Catalytic chemistry of iron-free Fenton nanocatalysts for versatile radical nanotherapeutics. *Materials Horizons* **2020**, *7* (2), 317-337.

(16) Wang, Y.; Waterhouse, G. I. N.; Shang, L.; Zhang, T. Electrocatalytic Oxygen Reduction to Hydrogen Peroxide: From Homogeneous to Heterogeneous Electrocatalysis. *Advanced Energy Materials* **2020**, *11* (15).

(17) Sun, Y.; Han, L.; Strasser, P. A comparative perspective of electrochemical and photochemical approaches for catalytic H_2O_2 production. *Chemical Society Reviews* **2020**, *49* (18), 6605-6631.

(18) Kofuji, Y.; Ohkita, S.; Shiraishi, Y.; Sakamoto, H.; Ichikawa, S.; Tanaka, S.; Hirai, T. Mellitic Triimide-Doped Carbon Nitride as Sunlight-Driven Photocatalysts for Hydro*gen Peroxide Production. ACS Sustainable Chemistry & Engineering 2017, 5 (8),* 6478-6485.

(19) Hou, H.; Zeng, X.; Zhang, X. Production of Hydrogen Peroxide by Photocatalytic Processes. *Angewandte Chemie International Edition* **2020**, *59* (40), 17356-17376.

(20) Zheng, Y.; Yu, Z.; Ou, H.; Asiri, A. M.; Chen, Y.; Wang, X. Black Phosphorus and Polymeric Carbon Nitride Heterostructure for Photoinduced Molecular Oxygen Activation. *Advanced Functional Materials* **2018**, *28* (10).

(21) Kofuji, Y.; Isobe, Y.; Shiraishi, Y.; Sakamoto, H.; Tanaka, S.; Ichikawa, S.; Hirai, T. Carbon Nitride–Aromatic Diimide–Graphene Nanohybrids: Metal-Free

Photocatalysts for Solar-to-Hydrogen Peroxide Energy Conversion with 0.2% Efficiency. *Journal of the American Chemical Society* **2016**, *138* (31), 10019-10025.

(22) Teng, Z.; Zhang, Q.; Yang, H.; Kato, K.; Yang, W.; Lu, Y.-R.; Liu, S.; Wang, C.; Yamakata, A.; Su, C.; et al. Atomically dispersed antimony on carbon nitride for the artificial photosynthesis of hydrogen peroxide. *Nature Catalysis* **2021**, *4* (5), 374-384

(23) Xia, Y.; Zhao, X.; Xia, C.; Wu, Z.-Y.; Zhu, P.; Kim, J. Y.; Bai, X.; Gao, G.; Hu, Y.; Zhong, J.; et al. Highly active and selective oxygen reduction to H_2O_2 on boron-doped carbon for high production rates. *Nature Communications* **2021**, *12* (1).

(24) Zhang, T.; Schilling, W.; Khan, S. U.; Ching, H. Y. V.; Lu, C.; Chen, J.; Jaworski, A.; Barcaro, G.; Monti, S.; De Wael, K.; et al. Atomic-Level Understanding for the Enhanced Generation of Hydrogen Peroxide by the Introduction of an Aryl Amino Group in Polymeric Carbon Nitrides. *ACS Catalysis* **2021**, *11* (22), 14087-14101.

(25) Che, H.; Gao, X.; Chen, J.; Hou, J.; Ao, Y.; Wang, P. Iodide-Induced Fragmentation of Polymerized Hydrophilic Carbon Nitride for High-Performance Quasi-Homogeneous Photocatalytic H_2O_2 Production. *Angewandte Chemie International Edition* **2021**, *60* (48), 25546-25550.

(26) Wu, S.; Yu, H.; Chen, S.; Quan, X. Enhanced Photocatalytic H_2O_2 Production over Carbon Nitride by Doping and Defect Engineering. *ACS Catalysis* **2020**, *10* (24), 14380-14389.

(27) Li, G.; Fu, P.; Yue, Q.; Ma, F.; Zhao, X.; Dong, S.; Han, X.; Zhou, Y.; Wang, J. Boosting exciton dissociation by regulating dielectric constant in covalent organic framework for photocatalysis. *Chem Catalysis* **2022**. DOI: 10.1016/j.checat.2022.05.002.

(28) Wang, H.; Yang, C.; Chen, F.; Zheng, G.; Han, Q. A Crystalline Partially Fluorinated Triazine Covalent Organic Framework for Efficient Photosynthesis of Hydrogen Peroxide. *Angewandte Chemie International Edition* **2022**, *61* (19).

(29) Chu, C.; Zhu, Q.; Pan, Z.; Gupta, S.; Huang, D.; Du, Y.; Weon, S.; Wu, Y.; Muhich, C.; Stavitski, E.; et al. Spatially separating redox centers on 2D carbon nitride with cobalt single atom for photocatalytic H_2O_2 production. *Proceedings of the National Academy of Sciences* **2020**, *117* (12), 6376-6382.

(30) Y. Shiraishi, S. Kanazawa, Y. Kofuji, H. Sakamoto, S. Ichikawa, S. Tanaka, T. Hirai, Sunlight-Driven Hydrogen Peroxide Production from Water and Molecular Oxygen by Metal-Free Photocatalysts, Angewandte Chemie International Edition. 2014, 53, 13454-13459.

(31) Y. Kofuji, S. Ohkita, Y. Shiraishi, H. Sakamoto, S. Tanaka, S. Ichikawa, T. Hirai, Graphitic Carbon Nitride Doped with Biphenyl Diimide: Efficient Photocatalyst for Hydrogen Peroxide Production from Water and Molecular Oxygen by Sunlight, ACS Catalysis. 2016, 6, 7021-7029.

(32) Zhang, P.; Tong, Y.; Liu, Y.; Vequizo, J. J. M.; Sun, H.; Yang, C.; Yamakata, A.; Fan, F.; Lin, W.; Wang, X.; et al. Heteroatom Dopants Promote Two-Electron O_2 Reduction for Photocatalytic Production of H_2O_2 on Polymeric Carbon Nitride. *Angewandte Chemie International Edition* **2020**, *59* (37), 16209-16217.

(33) Wu, C.; Teng, Z.; Yang, C.; Chen, F.; Yang, H. B.; Wang, L.; Xu, H.; Liu, B.; Zheng, G.; Han, Q. Polarization Engineering of Covalent Triazine Frameworks for Highly Efficient Photosynthesis of Hydrogen Peroxide from Molecular Oxygen and Water. *Advanced Materials* **2022**. DOI: 10.1002/adma.202110266.

(34) Cheng, H.; Lv, H.; Cheng, J.; Wang, L.; Wu, X.; Xu, H. Rational Design of Covalent Heptazine Frameworks with Spatially Separated Redox Centers for High-Efficiency Photocatalytic Hydrogen Peroxide Production. *Advanced Materials* **2021**, *34* (7).

(35) Chen, L.; Wang, L.; Wan, Y.; Zhang, Y.; Qi, Z.; Wu, X.; Xu, H. Acetylene and Diacetylene Functionalized Covalent Triazine Frameworks as Metal-Free Photocatalysts for Hydrogen Peroxide Production: A New Two-Electron Water Oxidation Pathway. *Advanced Materials* **2019**, *32* (2).

(36) Shiraishi, Y.; Matsumoto, M.; Ichikawa, S.; Tanaka, S.; Hirai, T. Polythiophene-Doped Resorcinol–Formaldehyde Resin Photocatalysts for Solar-to-Hydrogen Peroxide Energy Conversion. *Journal of the American Chemical Society* **2021**, *143* (32), 12590-12599.

(37) Cao, J.; Wang, H.; Zhao, Y.; Liu, Y.; Wu, Q.; Huang, H.; Shao, M.; Liu, Y.; Kang, Z. Phosphorus-doped porous carbon nitride for efficient sole production of hydrogen peroxide via photocatalytic water splitting with a two-channel pathway. *Journal of Materials Chemistry A* **2020**, *8* (7), 3701-3707.

(38) M. I. Koukourakis, A. Giatromanolaki, J. Skarlatos, L. Corti, S. Blandamura, M. Piazza, K. C. Gatter, A. L. Harris, *Cancer Res.* **2001**, *61*, 1830

(39) Zheng, D.-W.; Li, B.; Li, C.-X.; Fan, J.-X.; Lei, Q.; Li, C.; Xu, Z.; Zhang, X.-Z. Carbon-Dot-Decorated Carbon Nitride Nanoparticles for Enhanced Photodynamic Therapy against Hypoxic Tumor via Water Splitting. *ACS Nano* **2016**, *10* (9), 8715-8722.

(40) Kim, J.; Cho, H. R.; Jeon, H.; Kim, D.; Song, C.; Lee, N.; Choi, S. H.; Hyeon, T. Continuous O_2-Evolving $MnFe_2O_4$ Nanoparticle-Anchored Mesoporous Silica Nanoparticles for Efficient Photodynamic Therapy in Hypoxic Cancer. *Journal of the American Chemical Society* **2017**, *139* (32), 10992-10995.

(41) Li, X.; Kwon, N.; Guo, T.; Liu, Z.; Yoon, J. Innovative Strategies for Hypoxic-Tumor Photodynamic Therapy. *Angewandte Chemie International Edition* **2018**, *57* (36), 11522-11531.

(42) Cheng, Y.; Kong, X.; Chang, Y.; Feng, Y.; Zheng, R.; Wu, X.; Xu, K.; Gao, X.; Zhang, H. Spatiotemporally Synchronous Oxygen Self-Supply and Reactive Oxygen Species Production on Z-Scheme Heterostructures for Hypoxic Tumor Therapy. *Advanced Materials* **2020**, *32* (11).

(43) Dai, W.; Shao, F.; Szczerbiński, J.; McCaffrey, R.; Zenobi, R.; Jin, Y.; Schlüter, A. D.; Zhang, W. Synthesis of a Two-Dimensional Covalent Organic Monolayer through Dynamic Imine Chemistry at the Air/Water Interface. *Angewandte Chemie* **2016**, *128* (1), 221-225.

(44) Matsumoto, M.; Dasari, R. R.; Ji, W.; Feriante, C. H.; Parker, T. C.; Marder, S. R.; Dichtel, W. R. Rapid, Low Temperature Formation of Imine-Linked Covalent Organic Frameworks Catalyzed by Metal Triflates. *Journal of the American Chemical Society* **2017**, *139* (14), 4999-5002.

(45) Peng, G.; Albero, J.; Garcia, H.; Shalom, M. A Water-Splitting Carbon Nitride Photoelectrochemical Cell with Efficient Charge Separation and Remarkably Low Onset Potential. *Angewandte Chemie International Edition* **2018**, *57* (48), 15807-15811.

(46) Huang, C.; Wen, Y.; Ma, J.; Dong, D.; Shen, Y.; Liu, S.; Ma, H.; Zhang, Y. Unraveling fundamental active units in carbon nitride for photocatalytic oxidation reactions. *Nature Communications* **2021**, *12* (1).

(47) Zhang, X.; Xie, X.; Wang, H.; Zhang, J.; Pan, B.; Xie, Y. Enhanced Photoresponsive Ultrathin Graphitic-Phase C_3N_4 Nanosheets for Bioimaging. *Journal of the American Chemical Society* **2012**, *135* (1), 18-21.

(48) Kumar, P.; Vahidzadeh, E.; Thakur, U. K.; Kar, P.; Alam, K. M.; Goswami, A.; Mahdi, N.; Cui, K.; Bernard, G. M.; Michaelis, V. K.; et al. C_3N_5: A Low Bandgap Semiconductor Containing an Azo-Linked Carbon Nitride Framework for Photocatalytic, Photovoltaic and Adsorbent Applications. *Journal of the American Chemical Society* **2019**, *141* (13), 5415-5436.

(49) Zhao, D.; Wang, Y.; Dong, C.-L.; Huang, Y.-C.; Chen, J.; Xue, F.; Shen, S.; Guo, L. Boron-doped nitrogen-deficient carbon nitride-based Z-scheme heterostructures for photocatalytic overall water splitting. *Nature Energy* **2021**, *6* (4), 388-397.

(50) Zhang, Y.; Antonietti, M. Photocurrent Generation by Polymeric Carbon Nitride Solids: An Initial Step towards a Novel Photovoltaic System. *Chemistry - An Asian Journal* **2010**,5, 1307–1311

(51) Li, Y.; Ouyang, S.; Xu, H.; Wang, X.; Bi, Y.; Zhang, Y.; Ye, J. Constructing Solid–Gas-Interfacial Fenton Reaction over Alkalinized-C_3N_4 Photocatalyst To Achieve Apparent Quantum Yield of 49% at 420 nm. *Journal of the American Chemical Society* **2016**, *138* (40), 13289-13297.